THE JOURNAL OF PHYSICAL CHEMISTRY LETTERS
A JOURNAL OF THE AMERICAN CHEMICAL SOCIETY

pubs.acs.org/JPCL

Letter

Evolution of Structural and Electronic Properties of $TiSe_2$ under High Pressure

H. Saqib, S. Rahman,* Yongsheng Zhao, C. Cazorla, D. Errandonea, Resta Susilo, Yukai Zhuang, yanwei Huang, Bin Chen,* and Ning Dai*

Cite This: *J. Phys. Chem. Lett.* 2021, 12, 9859–9867

ABSTRACT: A pressure-induced structural phase transition and its intimate link with the superconducting transition was studied for the first time in $TiSe_2$ up to 40 GPa at room temperature using X-ray diffraction, transport measurement, and first-principles calculations. We demonstrate the occurrence of a first-order structural phase transition at 4 GPa from the standard trigonal structure (S.G.$P\bar{3}m1$) to another trigonal structure (S-G-$P\bar{3}c1$). Additionally, at 16 GPa, the $P\bar{3}c1$ phase spontaneously transforms into a monoclinic $C2/m$ phase, and above 24 GPa, the $C2/m$ phase returns to the initial $P\bar{3}m1$ phase. Electrical transport results show that metallization occurs above 6 GPa. The charge density wave observed at ambient pressure is suppressed upon compression up to 2 GPa with the emergence of superconductivity at 2.5 GPa, with a critical temperature (T_c) of 2 K. A structural transition accompanies the emergence of superconductivity that persists up to 4 GPa. The results demonstrate that the pressure-induced phase transitions explored by the experiments along with the theoretical predictions may open the door to a new path for searching and controlling the phase diagrams of transition metal dichalcogenides.

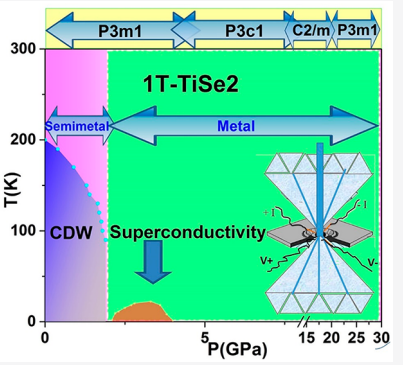

Transition metal dichalcogenides (TMDs) have attracted tremendous research interest over the past decade due to their interesting structural chemistry, unusual electronic properties, rich intercalation chemistry, and wide applications in 2D devices.[1,2] Phenomena such as the quantum Hall effect, superconductivity, and charge density wave (CDW) order have been discovered, stemming from the interplay of various correlations and instabilities in these systems.[3−6] TMDs share the chemical formula MX_2, where M is a transition metal (for instance, Mo, Ti, or W) and X is a chalcogenide atom (S, Se, or Te). Depending on the synthesis technique, the same composition of MX_2 can crystallize in diverse structures with very different electronic properties. Bulk TMDs can be metals, such as TaS_2 and $TaSe_2$, semimetals, such as $TiSe_2$, semiconductors, such as MoS_2, or insulators, such as HfS_2. Among TMDs, $TiSe_2$ is very important and has been broadly investigated because of its series of distinctive electronic properties ranging from CDW to superconductivity.[7−9] Layered $TiSe_2$, with a band gap (E_g) of 0.18 eV, is composed of stacked triatomic sheets where each triatomic monolayer exhibits a sandwiched structure with a plane of transition-metal titanium atoms covalently bonded to and sandwiched between two planes of chalcogen selenium atoms.[10−13] Pure $TiSe_2$ undergoes a commensurate CDW transition below $T \approx 200$ K with the formation of a super lattice ($2 \times 2 \times 2$).[14] The transition temperature of CDW is enhanced to ~232 K via thinning the sample to nanometers.[15]

Owing to its unique structural and electronic properties, $TiSe_2$ has been suggested as a substitute for graphene in thermoelectric applications and a cathode material in batteries.[3,16−19] Because $TiSe_2$ is a very suitable candidate material for optoelectronic applications, the research demands a significant way to adjust its band gap and electronic properties for the broad-scale use of this 2D material in photoelectric devices. Several recent studies suggest that strain or pressure can provide a clean and controllable way of tuning the band structures and electronic properties of 2D materials. Pressure is considered a powerful tool for manipulating crystal structures, either to tune the structure or physical properties of existing materials or as a route for the preparation of materials with structures unattainable at ambient pressure.[20,21]

Many cases show that the materials' superconducting behavior in the low-pressure (LP) region clearly differs from that at high pressures. The superconducting temperature (T_c) was found to be quite sensitive to pressure. There are various cases where the system has re-entered the superconducting stage at high pressure. In $PdSe_2$, the application of pressure systematically changed the transport properties, leading to pressure-induced metallization, and a superconducting state emerged upon the structural transition to the cubic pyrite

Received: July 30, 2021
Accepted: September 14, 2021

https://doi.org/10.1021/acs.jpclett.1c02492
J. Phys. Chem. Lett. 2021, 12, 9859−9867

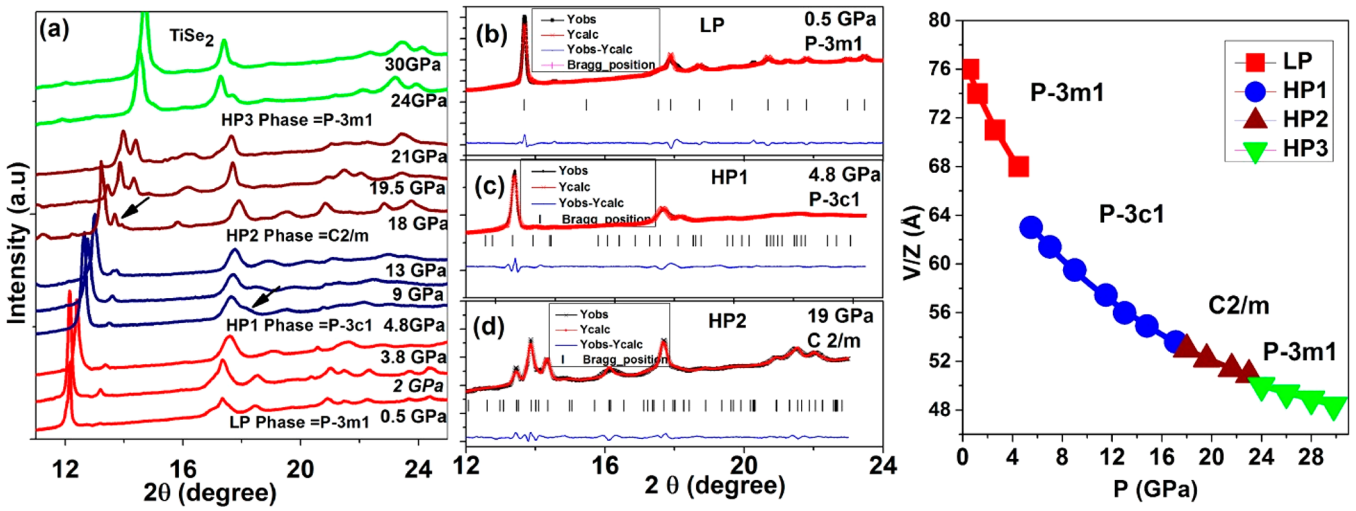

Figure 1. (a) Angle-dispersive XRD patterns for $TiSe_2$ at selected pressures at room temperature (λ = 0.4959 Å). Arrows indicate the appearance of new peaks. High-pressure X-ray diffraction patterns of $TiSe_2$ at room temperature (λ = 0.6199 Å). (b–d) Le Bail refinements for the low-pressure and new HP1 and HP2 phases at 0.5, 5.5, and 19 GPa, respectively. (e) Unit cell volume as a function of pressure for different phases.

phase above 6 GPa. A rapid increase in the T_c with compression was observed with a maximum T_c of 13.1 K at ~23 GPa, which is the highest T_c reported in TMDs to date.[22] Such studies motivated us to study $TiSe_2$ under compression for a more complete understanding of its properties.

Both Cu intercalation and the application of pressure in $TiSe_2$ have led to suppression of the transition temperature and ultimately the appearance of superconductivity.[9,23] Previous experimental high-pressure (HP) studies on 1*T*-$TiSe_2$ were limited to 8 GPa, in which the enhancement of T_{CDW} reached a maximum of ~1.1 K at 4 GPa.[9] In addition, there is only one reported HP Raman study of this material with a maximum pressure of just 20 GPa.[24] We also found little information about the HP transport properties at room temperature (RT). Thus it is crucial to carefully explore the HP behavior of 1*T*-$TiSe_2$ at higher pressures for a thorough understanding of this material. A comprehensive theoretical and experimental analysis of the structural and physical properties of $TiSe_2$ under high pressure has also never been reported. We have performed the first inclusive study of this vital TMD by combining experimental techniques, including HP X-ray diffraction (XRD), Raman spectroscopy, and transport measurements at RT and theoretical density functional theory (DFT) calculations. We also performed temperature-dependent resistivity measurements at high pressure for the observation of superconductivity. This study will provide the first definitive understanding of the structural changes in the $TiSe_2$ system and its correlation with the transport properties of this material under compression. Our HP XRD studies up to 35 GPa show the start of the structural transition from the ambient $P\bar{3}m1$ to a $P\bar{3}c1$ phase after 4 GPa. Then, at ~16 GPa, the $P\bar{3}c1$ phase changes to a monoclinic $C2/m$ phase, which spontaneously transitions to a phase with the same symmetry as the original $P\bar{3}m1$ phase at 24 GPa. Such re-entrant phase behavior is also confirmed from the DFT calculations. Raman spectroscopy and transport measurements confirm the structural changes. The HP phases are found to be metallic. Superconductivity was observed only in a narrow pressure range, that is, from 2.5 to 4 GPa. The applied pressure effectively enhances the conductivity and the carrier concentration, which ultimately makes $TiSe_2$ a suitable device for applications in strain-modulated optoelectronic devices.

Single-crystal samples of 1*T*-$TiSe_2$ used for HP experiments were purchased from HQ Graphene. We performed HP-XRD measurements for 1*T*-$TiSe_2$ at the Shanghai Synchrotron Radiation Facility (SSRF, BL15U1 beamline), China, with an X-ray wavelength of 0.6199 Å. HP conditions were obtained with a diamond anvil cell (DAC), using silicon oil as a pressure-transmitting medium. Sample pressures were determined using the calibrated ruby pressure standard of Mao et al.[25] XRD patterns were collected using a Mar165 charge-coupled device (CCD) detector. The resulting ring-type diffraction patterns were integrated using the Fit2D software. Le Bail refinement analyses were carried out using the FullProf software.[26]

Raman spectroscopy experiments were completed using an inVia Renishaw Raman spectrometer system with a laser wavelength of 532 nm and a 2400 g/cm grating. Our range of interest was 100–400 cm^{-1}. Like in XRD, we used silicon oil as a pressure-transmitting medium during measurements under HP. The wavenumbers of the Raman peaks were determined with an accuracy of 1 cm^{-1}. HP electrical resistivity measurements were performed using the standard four-probe technique in a DAC up to 35 GPa. The gasket was insulated with a mixture of epoxy and cubic boron nitride. Four platinum leads were arranged to contact the sample in the chamber. No pressure medium was used for the resistivity measurement. The resistance was determined by the Van der Pauw method.[27]

First-principles calculations based on DFT[28] were performed to theoretically analyze the structural, vibrational, and electronic properties of $TiSe_2$ under pressure. The meta-GGA SCAN exchange-correlation functional[29] was employed for most calculations because it is implemented in the VASP package.[30] The "projector augmented wave" method was employed to represent the ionic cores,[31] and we considered the following electrons as valence: 3d and 4s of Ti and 4s and 4p of Se. Wave functions were represented in a plane-wave basis truncated at 650 eV, and for integrations within the first Brillouin zone, a gamma-centered **k**-point grid of 14 × 16 × 10 was employed. Geometry relaxations were performed by imposing a tolerance on the atomic forces of 0.005 eV·$Å^{-1}$.

https://doi.org/10.1021/acs.jpclett.1c02492
J. Phys. Chem. Lett. 2021, 12, 9859–9867

Table 1. Lattice Parameters and Profile-Matching Parameters of the Cubic and the High-Pressure Phases[a]

		lattice constant parameters			profile-matching parameters		
phase	P (GPa)	a (Å)	b (Å)	c (Å)	R_p (%)	R_{wp} (%)	χ^2
trigonal $P\bar{3}m1$	0.5	4.210763 (1)	4.210763 (1)	4.974298 (1)	1.18	1.41	0.97
trigonal $P\bar{3}c1$	5.5	7.044479 (2)	7.044479 (2)	11.329847 (2)	1.41	1.78	1.62
monoclinic $C2/m$	19	17.562742 (3)	3.276016 (3)	5.426599 (3)	1.80	1.93%	1.89
trigonal $P\bar{3}m1$	24	3.08760 (3)	3.08760 (3)	6.11930 (3)	1.30	1.33	1.32

[a]β angle of the monoclinic phase is 91.18°.

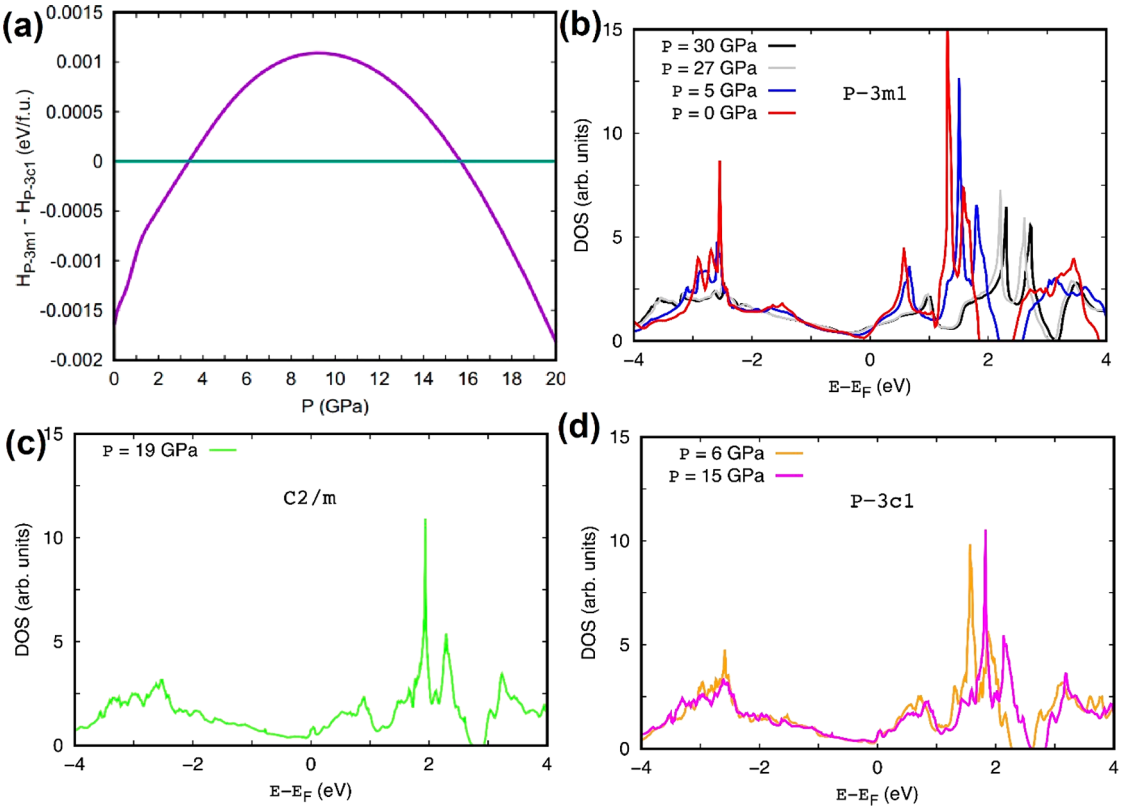

Figure 2. (a) Enthalpy curves are estimated with density functional theory (DFT) techniques and expressed as a function of pressure. The narrow pressure range in which the stable structure is the monoclinic $C2/m$ phase, namely, $11.2 \leq P \leq 13.8$ GPa, is not indicated in the figure. (b–d) Calculated density of electronic states for bulk $TiSe_2$ at several pressures and for different crystal structures.

The obtained energies were converged to within 0.5 meV per formula unit by using these technical parameters.

Zero-temperature phonon frequencies were estimated with the small-displacement method, in which the force constant matrix is calculated in real space by considering the proportionality between atomic displacements and forces.[32] The quantities that our phonon calculations need to converge with include the size of the supercell, the size of the atomic displacements, and the numerical accuracy in the sampling of the Brillouin zone. We found the following settings to provide quasi-harmonic free energies converged to within 5 meV per formula unit: 4 × 4 × 4 supercells (the figures indicate the number of unit cell replicas along the corresponding lattice vectors), atomic displacements of 0.02 Å, and $\boldsymbol{q}$-point grids of 16 × 16 × 16. The value of the phonon frequencies, ω_{qs}, was obtained with the PHON code developed by Alfè.[33] Using this software, we exploited the translational invariance of the system to impose the three acoustic branches to be exactly zero at the center of the Brillouin zone and applied central differences in the atomic forces.

To explore the thermodynamic stability of pristine 1T-$TiSe_2$ under high pressure, we performed synchrotron XRD measurements at RT up to 30.0 GPa, as shown in Figure 1. Because of the strong preferred orientation of the compressed sample, all XRD patterns were analyzed using the Le Bail method.

Pristine 1T-$TiSe_2$ crystallizes in a trigonal structure with the space group $P\bar{3}m1$ at ambient pressure. Under compression up to 3 GPa, there was no major change found in the XRD patterns except a gradual shift of the Bragg peaks toward higher angles, and all patterns were identified with the $P\bar{3}m1$ phase, as shown in Figure 1b. The Le Bail analysis of powder XRD patterns at 0.5 GPa indicates the pure trigonal $P\bar{3}m1$ phase, as shown in Figure 1b. The resulting lattice parameter are $a = b =$ 4.210 Å and $c = 4.974$ Å, with profile-matching parameters R_p = 1.86%, R_{wp} = 1.23%, and χ^2 = 1.4, which are in good agreement with the previous report.[13]

Beyond 3.5 GPa, extra diffraction peaks indicated by arrows start to appear, suggesting the onset of a structural phase transition. Finally, at ∼4 GPa, we observe a structural phase transition from the $P\bar{3}m1$ to a $P\bar{3}c1$ phase. Representative Le

https://doi.org/10.1021/acs.jpclett.1c02492
J. Phys. Chem. Lett. 2021, 12, 9859−9867

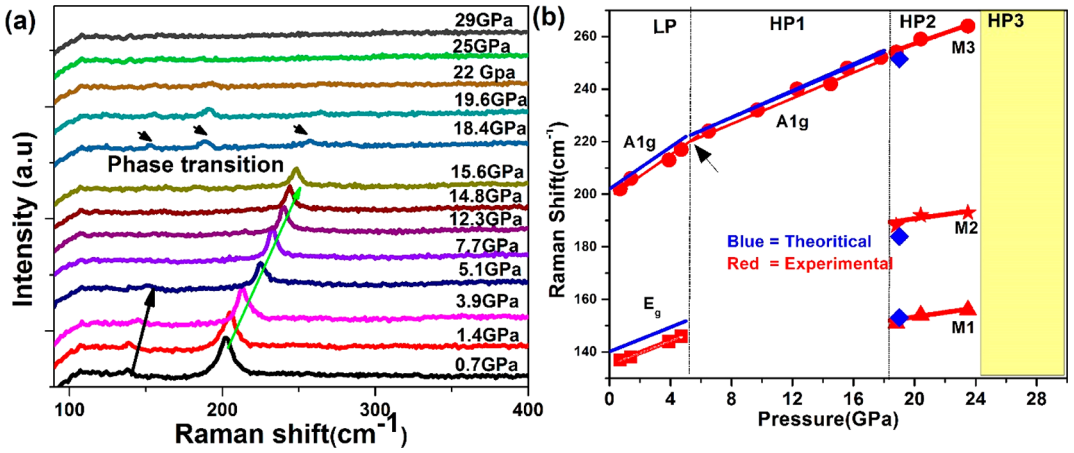

Figure 3. (a) Raman spectra of $TiSe_2$ from 0 to 25 GPa showing the Raman mode disappearing at the first phase transition (~5.5 GPa). (b) Comparison between the experimental and calculated modes' frequencies.

Bail refinements of the HP-XRD patterns at 5.5 GPa are illustrated in Figure 1c. Interestingly, at ~16 GPa, the $P\bar{3}c1$ phase spontaneously transitions to the $C2/m$ phase, as shown in Figure 1d. This phase returns to the ambient $P\bar{3}m1$ phase after 24 GPa, as shown in Figure S3. The $P\bar{3}m1$ phase stabilizes again up to the highest pressure we attained in our study. Our theoretical calculations also predict the existence of a $P\bar{3}m1-P\bar{3}c1-C2/m-P\bar{3}m1$ structural phase sequence.

From the experiments, we determined the pressure dependence of the volume for different phases. Discontinuities in the volume indicate that the first and third transitions are first-order transformations. In the second transition, there is no detectable volume discontinuity. Because $C2/m$ is a maximal subgroup of $P\bar{3}c1$, the second transition could have a second-order nature. The unit-cell volume as a function of pressure was fitted with the following third-order Birch–Murnaghan equation of state[34,35]

$$P = \frac{3}{2}K_0[(V_0/V)7/3 - (V_0/V)5/3][1 - (3/4)(4 - K_0')[(V_0/V)2/3 - 1)] \quad (1)$$

where P and V are the measured pressure and unit cell volume, respectively, K_0 is the bulk modulus, K_0' is the first pressure derivative of the bulk modulus, and V_0 is the unit cell volume under ambient conditions. The fits give $K_0 = 31(4)$ GPa, $K_0' = 4.0$, and $V_0 = 78(5)$ Å^3 for the LP trigonal phase, $K_0 = 33(5)$ GPa and $K_0' = 4.0$ for the HP1 trigonal phase, and $K_0 = 41(5)$ GPa and $K_0' = 4.0$ for the HP2 monoclinic phase, whereas they give $K_0 = 47(4)$ GPa and $K_0' = 4.0$ for the HP4 phase trigonal phase, where P and V are the measured pressure and unit cell volume, respectively, as shown in the Figure 1e.

The profile-matching parameters and lattice constant parameters of both LP and HP phases (HP1, HP2) obtained from the profile Le Bail refinements are given in Figure 1b–d and Table 1. The Le Bail fit for the HP3 phase is shown in Figure S1. Upon releasing pressure to ambient, the original ambient phase is recovered. Hence the phase transition is confirmed to be reversible.

To obtain a deeper insight into the nature of the structural changes found in our experimental results, we performed first-principles DFT calculations. The enthalpy curves computed for bulk $TiSe_2$ are shown in Figure 2a. It can be appreciated that the stable phase from ambient pressure up to ~3.4 GPa is the hexagonal $P\bar{3}m1$. At larger pressures, the crystal is stabilized in the hexagonal $P\bar{3}c1$ phase, which subsequently spontaneously transforms (i.e., in a continuous second-order fashion) into the monoclinic $C2/m$ phase at a theoretical pressure of 11.2 GPa. This space group is a subgroup of $P\bar{3}c1$, and the enthalpy differences between the two phases are very small in comparison with the differences in the enthalpy of the $P\bar{3}m1$ phase. The monoclinic $C2/m$ phase subsequently transforms into the hexagonal $P\bar{3}m1$ phase at a theoretical pressure of 15.8 GPa when the former structure becomes vibrationally unstable. Thus the monoclinic $C2/m$ phase appears to act as a structural bridge between the hexagonal phases $P\bar{3}c1$ and $P\bar{3}m1$. Therefore, the reentrant phase behavior observed in the experiments is fully confirmed by the theoretical enthalpy curves shown in Figure 2a; however, we appreciate that the DFT calculations tend to systematically underestimate the experimental transition pressures. This is probably due to neglecting temperature effects and dispersion long-range interactions in the simulations.

Raman spectroscopy is a sensitive technique for detecting subtle structural changes and chemical reactivity. Therefore, it is suitable to shed light on the observed phase transitions in $TiSe_2$. A Raman spectroscopy measurement under pressure was employed up to 30 GPa, as shown in Figure 3a. The group-theoretical analysis for 1T-$TiSe_2$ predicts the presence of nine zone-center vibrational modes $A_{1g} + 2A_{2u} + 2E_u + E_g$.[36] The degenerated E_g mode and the A_{1g} mode are Raman-active modes, whereas one degenerated E_u and one A_{2u} mode are infrared (IR)-active modes. The remaining modes are acoustics modes. The Raman-active A_{1g} mode arises due to the out-of-plane vibration of the stretching of two Se atoms moving relative to one another along the z axis, whereas the E_g mode represents the symmetric in-plane bending of the Se atoms along the xy directions.

We calculated the Raman- and IR-active phonon frequencies and also phonon dispersions, which are shown, as an example for the $P\bar{3}m1$ and $P\bar{3}c1$ phase, in the Supporting Information (Figure S4), showing their dynamical stability. The calculated Raman frequencies will be used to assign the mode symmetry of measured Raman modes. On the basis of our theoretical calculations and the existing literature, the peaks obtained for the ambient spectrum at around 137 and 202 cm^{-1} are assigned to the E_g and A_{1g} modes, respectively. These results are similar to the previous studies under ambient conditions.[37]

https://doi.org/10.1021/acs.jpclett.1c02492
J. Phys. Chem. Lett. 2021, 12, 9859–9867

Table 2. Calculated and Experimental Raman Modes with Corresponding dw/dP and Mode Grüneisen Parameters

low-pressure phase (LP)				high-pressure phase 1 (HP1)				high-pressure phase 2 (HP2)			
Raman modes experimental ω_o (cm^{-1})	Raman modes calculated ω_o(cm^{-1})	dω/dP (cm^{-1}/GPa)	γ	Raman modes ω_o (cm^{-1})	Raman modes calculated ω_o(cm^{-1})	dω/dP (cm^{-1}/GPa)	γ	Raman modes ω_o (cm^{-1})	Raman modes calculated ω_o(cm^{-1})	dω/dP (cm^{-1}/GPa)	γ
139.2	140	1.86	0.45	210	139.2	1.12	0.5	212	210	1.12	0.5
201	200	2.97, 2.64	0.36					180	183	1.05	0.38
								145	143	1.7	0.42

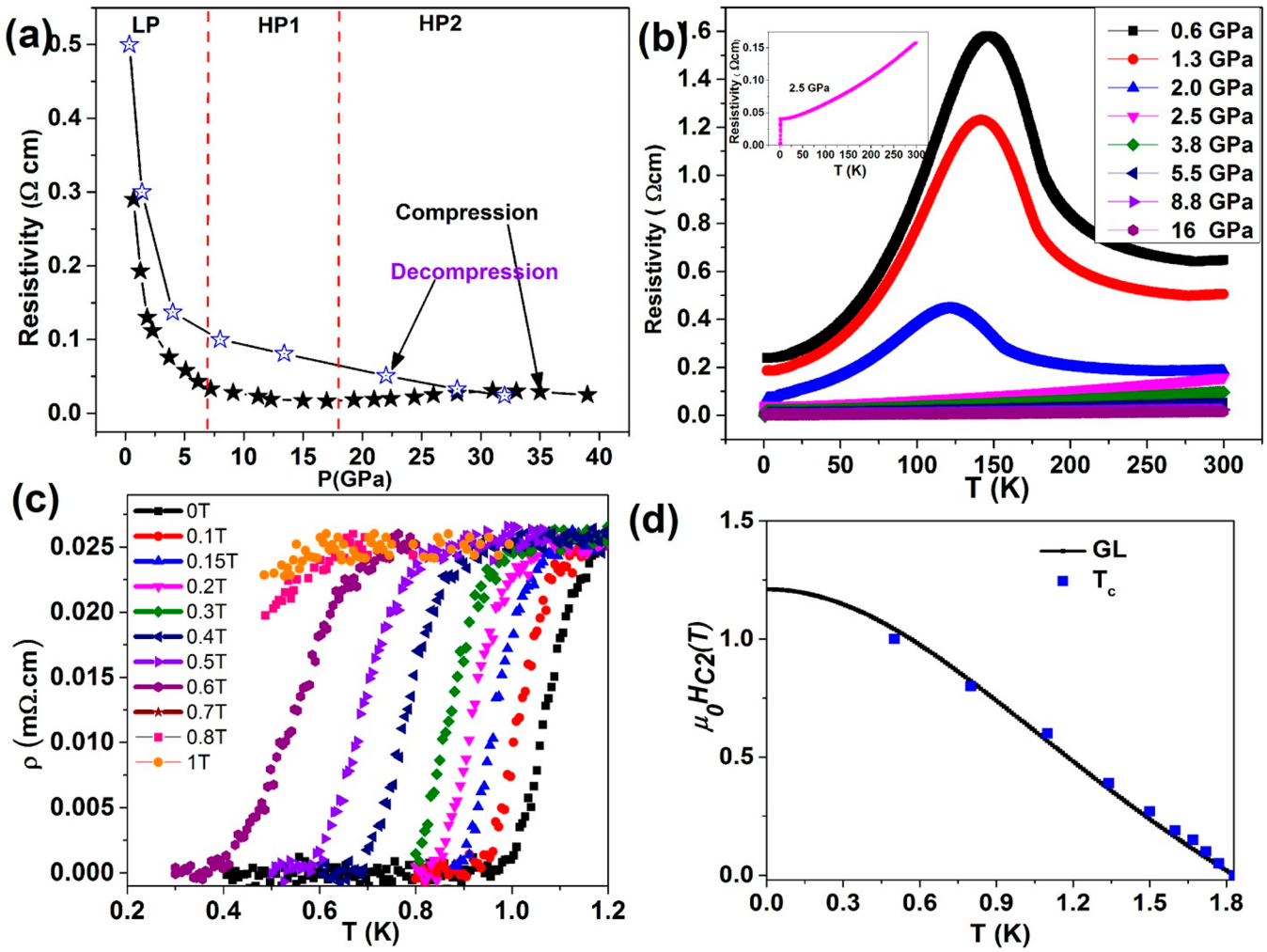

Figure 4. Electrical resistance behavior of $TiSe_2$ as a function of pressure at RT. (b) Temperature−resistivity curves at different pressures. (c). Temperature dependence of resistivity under different magnetic fields at 3.8 GPa. (d) $\mu_0 H_{c2}-T$ phase diagram, where the solid line represents fitting by the Ginzburg−Landau (GL) equation.

Our LP phase results are similar to those of Rajaji et al.; however, they were unable to explore the Raman measurements at higher pressure.[24] We also confirmed our experimental results by theoretical analysis, as discussed later in this section.

As the pressure increases, the intensity of the A_{1g} and E_g modes decreases along with the gradual shift toward higher frequencies. With compression, the peak intensity of the E_g mode rapidly decreases and completely disappears above 5 GPa. This mode has very little intensity from the beginning of the experiment. Thus with the further reduction in intensity, it was not possible to follow the E_g mode above ∼6 GPa. This disappearance of the E_g mode is indicative of the first phase transition. Our structural analysis through XRD also indicates the first phase transition in this pressure range.

Our DFT calculations proposed various modes for the first high-pressure (HP1) phase. This phase has 5 A_{1g} and 12 E_g Raman-active modes, whereas there are 17 IR-active modes, including 6 A_{2u} and 11 E_u modes. Owing to the low scattering factor and the reduced thickness of the sample, we observed only the strongest A_{1g} mode in our experiment.

Figure 3a shows that the three new modes (M1, M2, and M3) that appear above 16 GPa represent another phase transition (labeled as HP2), as corroborated by our XRD studies. The increase in the number of modes is consistent with the occurrence of the HP1−P2 transition. Our theoretical

https://doi.org/10.1021/acs.jpclett.1c02492
J. Phys. Chem. Lett. 2021, 12, 9859−9867

calculations predicted the presence of the following modes for the second HP2 $C2/m$ phase

Raman-active modes: 4 A_g + 2 B_g

infrared-active modes: 3 A_u + 6 B_u

We observed three of the six Raman modes mentioned above. According to our performed DFT calculations, the $C2/m$ phase is found to be stable in a small pressure range of ∼4.6 GPa, so we have the phonons for this phase at only one pressure value. Good agreement exists between the observed and calculated Raman modes, as shown in Figure 3b. All of the Raman modes disappear by increasing the pressure beyond 24 GPa, which signposts the phase transition. Our XRD experiments also indicate the presence of a phase transition beyond 24 GPa.

In general, when pressure increases, we observe a monotonous increase (hardening) in Raman frequencies. Any deviation in this suggests changes in the structure or electronic properties of the material. In our case, all of the modes seem to harden with increasing pressure, as expected. Nevertheless, there are distinct changes in the evolution of Raman frequencies as a function of pressure, which are important to signify transitions in the 1T-$TiSe_2$ system.

There are subtle changes in the pressure dependence of the A_{1g} mode frequency, which is the most intense Raman peak of 1T-$TiSe_2$ (phase) and the HP phase. By using the linear fit equation $\omega(P) = \omega(P_0) + a_1(P - P_0)$ to determine the slope ($a_1 = d\omega/dP$) of the A_{1g} mode frequency in Figure 3b, we observe a distinct change in the slopes of the pressure at ∼6 GPa. Such changes in the slope and the disappearance of the E_g mode of the phase point toward the structural change.

The mode frequencies of all of the observed Raman modes, pressure coefficients $\left(\frac{d\omega}{dP}\right)$, and calculated Grüneisen parameters are shown in Table 2. The mode Grüneisen parameters (γ) were obtained for the LP, HP1, and HP2 phases with the equation $\gamma = K_0/\omega_0(d\omega/dP)$ by using the bulk modulus (K_0) determined from the XRD data. The values of the Grüneisen parameters for the LP, HP1, and HP2 phases ranged from 0.36 to 0.45, to 0.5, to 0.38 to 0.5, respectively. The obtained mode Grüneisen parameters can be used to determine the heat capacities and vibrational entropies using the Kieffer model.[38]

The layered 1T-$TiSe_2$ is a semimetal with an indirect band gap of 0.18 eV, where the different layers are interconnected through a van der Waals interaction and can be exfoliated into atomically thin layers. Note that our DFT calculations predict a metallic ground state for $TiSe_2$ within the entire range of investigated pressures; see Figure 2b−d. This outcome indicates that our first-principles calculations tend to underestimate the small energy band gap of $TiSe_2$, which is a well-known drawback of standard DFT approaches. Here we present the effect of pressure on the evolution of the electronic behavior of this material. Figure 4a shows our new finding of resistivity as a function of pressure.

The pressure-dependent resistivity of $TiSe_2$ was obtained up to 40 GPa. Figure 4a depicts the electrical resistivity (ρ) of $TiSe_2$ as a function of P at RT. The pressure-dependent room-temperature electrical resistivity on $TiSe_2$ reveals a sharp decrease in the resistivity from ambient pressure to ∼4 GPa. Such a sharp drop in the resistivity may be due to the structural phase transition indicated by our XRD measurement. With further compression, the resistivity shows a gradual decrease to 13 GPa, after which it becomes almost pressure-independent for the region 12 < P < 20 GPa. Our HP XRD and Raman spectroscopy results both show a second structural phase transition in this region.

The resistivity of the HP monoclinic phase is smaller to that of the trigonal phase. At a low pressure of ∼4.5 GPa, the resistivity sharply decreases to a minimum. Our HP−XRD results confirmed that the ambient trigonal phase began transforming to the trigonal $P\bar{3}c1$ phase at this pressure.

The extremely low resistivity in the HP2 region after 24 GPa exhibits a typical metallic behavior. Above 25 GPa, the change in resistance is negligible, and it becomes/remains almost pressure-independent with the further rise in pressure. The order of magnitude of the electrical resistivity of the trigonal phase and the monoclinic HP phase at ambient temperature changes from R = 0.5 to 0.04 Ω cm and from R = 0.5 to 0.03 Ω cm, respectively. The reduction in the bond distances might be one reason for these changes.

The sample was decompressed by gradually decreasing the pressure. Complete decompression results in a relatively higher initial value of resistivity than that of the ambient phase, which may be due to some defect after decompression from the HP phase.

To achieve a more comprehensive understanding of the electrical properties, we measured the temperature-dependent resistivity further from 0.7 to 2.2 GPa, as shown in Figure 4b. The resistivity curves up to 1.1 GPa are like those at ambient pressure. The sharp curvature in resistivity is indicative of the CDW transition. $TiSe_2$ was one of the first known CDW-bearing compounds and is also one of the most frequently studied, although the nature of its CDW transition has been controversial for decades. In our case, the CDW transition temperature, T_{CDW}, identified from the maximum of $-d\rho(T)/dT$, gradually shifts to a lower temperature with compression. At the same time, the resistivity anomalies that correspond to the CDW transition are weakened with increasing pressure. It is clearly shown that the application of pressure suppresses the phase transition and that the associated resistivity anomaly becomes much less prominent. In this pressure range, the resistivity above the transition represents weak nonmetallic temperature dependence. At temperatures well below the transition, the electrons that uncondense into the CDW give a metallic character to the resistivity. There are various cases where CDW transitions ultimately lead to the appearance of superconductivity.

The further application of pressure gives rise to a metallic high-temperature region where the resistivity behaves linearly with temperature. At the same time, we observed a monotonous decrease in the CDW transition temperature that ultimately becomes difficult to identify above 2.5 GPa and disappears completely above 3 GPa from our resistivity measurements. In the pressure range of 2−4 GPa, we observed superconductivity at a low temperature, where T_c = 1 K at 3 GPa, then increases slightly to 1.5 K at 3.5 GPa.

On the basis of theoretical studies by Koley et al., the preformed excitons in normal state $TiSe_2$ drive the compound to undergo a CDW superconducting phase transition under pressure.[39]

This indicates that the influence of pressure on the transition is not primarily through the change in the size or shape of the Fermi surface but must be through the stiffening of the lattice force constants. It was suggested that the pressure dependence of the transition is stronger than that expected from the Fermi surface changes alone, and hence the phonon-driven model by

https://doi.org/10.1021/acs.jpclett.1c02492
J. Phys. Chem. Lett. 2021, 12, 9859−9867

White and Lucovsky can be favored for the structural distortion in $TiSe_2$.[40]

To confirm the appearance of superconductivity in the compressed $TiSe_2$, we performed resistivity measurements under different applied magnetic fields at 3.8 GPa, as shown in Figure 4c. Superconductivity in pure 1*T*-$TiSe_2$ is highly sensitive to the magnetic field, which is in sharp contrast with the Cu intercalated system Cu_xTiSe_2.[9,23] Zero resistance at 3.8 GPa gradually lifts as the applied magnetic field increases. Simultaneously, the T_c value decreases toward a low temperature, and the superconducting transition is gradually suppressed by the increasing magnetic field.

In Figure 4d, we show the upper critical field, H_{c2}, determined from the onset of the resistivity drop. The H_{c2} versus T_c curve was then fitted with the empirical expression based on the Ginzburg–Landau (GL) theory (e.g., ref 41) which takes the form of

$$\mu_0 H_{c2}(T) = \mu_0 H_{c2}(0)\frac{1-\left(\frac{T}{T_c}\right)^2}{1+\left(\frac{T}{T_c}\right)^2}$$

The data in Figure 4b can be well-fitted using the above equation. The value of $\mu_0 H_{c2}(0)$ at 3.8 GPa is determined to be 1.22 T. This value is smaller than the $\mu_0 H_{c2}(0)$ value of $TiTe_2$, for example, >10 T,[42] but higher than the Bardeen–Cooper–Schrieffer (BCS) Pauli limit $\mu_0 H_P = 1.86 \times T_c(0)$ of 2.8 T.

Pressure or compressive strain is known to be a powerful and clean way to continuously tune the crystal and electronic structures in TMDs. Because of the weak interlayer van der Waals interaction, the interlayer van der Waals bonding in 2D TMD is highly compressible. Therefore, it can be expected that pressure or compressive strain will introduce a dramatic shortening of this interlayer bonding, thereby enhancing the electronic interactions between the layers. Our XRD experiment illustrates a phase transition from a trigonal $P\bar{3}m1$ to a $P\bar{3}c1$ phase that ultimately changes to a monoclinic $c2/m$ phase at 5 and 16 GPa, respectively. We observed a reentrant phase behavior where the $C2/m$ phase transitions back to the original $P\bar{3}m1$ phase. We confirmed the reliability of the occurrence of such a transition sequence under pressure through DFT calculations.

A phase diagram of 1*T*-$TiSe_2$ summarizes all of the results under nonhydrostatic compressions (Figure 5). The CDW is seen in a pressure range from ambient to 2 GPa, where our XRD data did not show any structural change in this pressure range. Our Raman measurements also did not point toward any structural transition in this region. Gradual shifting in the peak is merely due to compression. Therefore, we can conclude that the CDW transition does not affect the structural properties of $TiSe_2$. From 2 to 4 GPa, superconductivity is observed. Our Raman and XRD measurements indicate the presence of a first-order structural phase transition. Similarly, transport measurements also show a rapid decrease in the resistivity for this pressure region after 4 GPa. A slight difference in pressure points may be due to the nonhydrostatic conditions in the transport measurements. In addition, after 16 GPa, another phase transition is observed from the XRD and Raman measurements. The reentrant phase behavior is seen in the XRD measurements.

Lattice instability and structural fluctuation have been generally observed in TMDs through XRD, electron

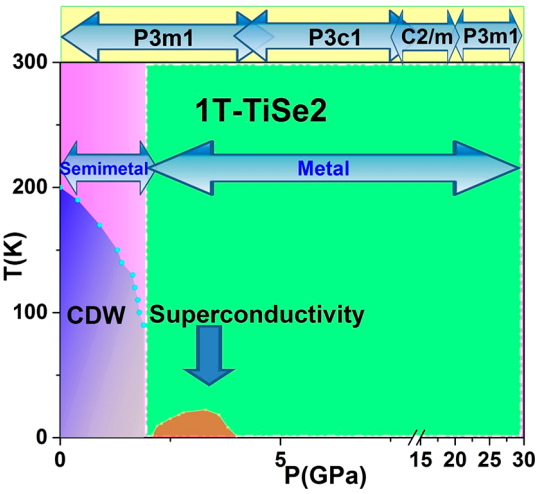

Figure 5. Phase diagram for 1*T*-$TiSe_2$. The vertical blue and green shades demarcate the semimetal and metallic states, respectively.

diffraction, and temperature-dependent resistivity measurements, suggesting a close connection between the lattice degrees of freedom and superconductivity. There are various studies on TMDs where superconductivity has been associated with a structural phase transition. Chi et al. investigated the crystal structure and electrical resistivity of $2H_c$-MoS_2 under pressure of up to 160 GPa and observed a pressure-induced $2H_c$-to-$2H_a$ polytype transformation near 30 GPa accompanied by a semiconductor-to-metal transition.[43] The 2Ha phase exhibited superconductivity at pressures beyond 90 GPa. A dramatic increase in the T_c was observed from 5 to 12 K. There are various other examples where the emergence of superconductivity is associated with the structural phase transition. $ZrTe_5$ clearly reveals the semimetal-to-superconductor transition at ∼6 GPa, which is related to the phase transition from *Cmcm* to $C2/m$.[43] Unlike MoS_2, $MoTe_2$ exhibits a semiconductor-to-metallic transition by the gradual tuning of the electric structure and band gap without a structural transition.[44] In our current work, superconductivity emerges in $TiSe_2$ as the CDW transition is suppressed above ∼2 GPa. Interestingly, superconductivity only appears in a narrow pressure region, that is, between 2 and 4 GPa. Our XRD data reveal a structural phase transition from the trigonal $P\bar{3}m1$ to the trigonal $P\bar{3}c1$ above 4 GPa, which suggests that the pressure-induced superconductivity in $TiSe_2$ appears in the $P\bar{3}m1$ phase. In an isostructural $TiTe_2$, the superconductivity emerges together with the formation of the HP monoclinic $C2/m$ phase.[42] By comparison, the structural transition to the $P\bar{3}c1$ phase above 4 GPa destroys the superconductivity in $TiSe_2$, which indicates that this phase is unfavorable for hosting superconductivity. We observed that the pressure derivative of the $TiSe_2$ CDW transition temperature is negative, like the similar experimental observation by Kusmartseva et al.[9]

The CDW fluctuations are tightly linked to superconductivity in 1*T*-$TiSe_2$. This behavior is comparable to that of several families of materials where the superconducting dome has been discovered in the vicinity of the purely electronic-ordered phase. Addressing the quantum critical point strengthens the viewpoint of excitonic superconductivity in 1*T*-$TiSe_2$.[45,46] On the contrary, the continuous development of the soft phonon mode in the vicinity of the CDW transition, in both Cu-intercalated and pure and pressurized material,[9]

https://doi.org/10.1021/acs.jpclett.1c02492
J. Phys. Chem. Lett. 2021, 12, 9859−9867

suggests that the lattice deformation may not be regarded as a secondary effect that simply follows the electronic ordering.

The transition is ascribed to the Se 4p and Ti 3d band inversion with different parities at the C-point. It is very likely that the pressure range where the topologically nontrivial phase emerges overlaps with the state where the superconductivity emerges, which might lead to a self-induced topological surface superconductivity in pressurized 1*T*-$TiSe_2$. However, in our studies, we also observed that the superconductivity transition is related to the structural phase transition.

In conclusion, $TiSe_2$ undergoes a pressure-induced phase transition from the $P\bar{3}m1$ to a $P\bar{3}c1$ phase near 4 GPa, and at ∼16 GPa, the $P\bar{3}c1$ phase changes to a $C2/m$ phase. Interestingly, this $C2/m$ phase transitions back to the original $P\bar{3}m1$, which again stabilizes up to 35 GPa, the highest pressure reached in our study. Such reentrant phase behavior was carefully studied through Raman and transport measurements. Metallic behavior was determined for the three HP phases through the temperature-dependent resistivity and *ab initio* calculations. Superconductivity was observed in the sample at 2.5 GPa. The extensive and continuous tuning of its electronic structure can be potentially used for energy-variable (IR-visible) optoelectronics and photovoltaics applications.

■ ASSOCIATED CONTENT

Supporting Information

The Supporting Information is available free of charge at https://pubs.acs.org/doi/10.1021/acs.jpclett.1c02492.

Figures providing decompression of high-pressure Raman spectroscopy, decompression of high-pressure XRD, structure refinement of the HP3 phase, and partial density of states (PDOS) of the high-pressure phases at different pressures (PDF)

■ AUTHOR INFORMATION

Corresponding Authors

Bin Chen − *Center for High Pressure Science and Technology Advanced Research, Shanghai 201203, China*; Email: chenbin@hpstar.ac.cn

Ning Dai − *Shanghai Institute of Technical Physics, Chinese Academy of Science, Shanghai 201800, China; School of Physics and Optoelectronic Engineering, Hangzhou Institute for Advanced Study, UCAS, Hangzhou 310024, China*; Email: ndai@mail.sitp.ac.cn

S. Rahman − *Center for High Pressure Science and Technology Advanced Research, Shanghai 201203, China; School of Physics and Optoelectronic Engineering, Hangzhou Institute for Advanced Study, UCAS, Hangzhou 310024, China*; orcid.org/0000-0002-3039-7817; Email: saqibrahman@ucas.edu.cn

Authors

H. Saqib − *Center for High Pressure Science and Technology Advanced Research, Shanghai 201203, China; Shanghai Institute of Technical Physics, Chinese Academy of Science, Shanghai 201800, China*

Yongsheng Zhao − *Center for High Pressure Science and Technology Advanced Research, Shanghai 201203, China*

C. Cazorla − *Departament de Física, Universitat Politècnica de Catalunya, Barcelona 08034, Spain*; orcid.org/0000-0002-6501-4513

D. Errandonea − *Departamento de Física Aplicada-ICMUV, MALTA Consolider Team, Universidad de Valencia, Edificio de Investigación, Valencia 46100, Spain*; orcid.org/0000-0003-0189-4221

Resta Susilo − *Center for High Pressure Science and Technology Advanced Research, Shanghai 201203, China*

Yukai Zhuang − *Institute of Atomic and Molecular Physics, Sichuan University, Chengdu 610065, China*

yanwei Huang − *State Key Laboratory of Precision Spectroscopy, East China Normal University, Shanghai 200062, China*

Complete contact information is available at: https://pubs.acs.org/10.1021/acs.jpclett.1c02492

Notes

The authors declare no competing financial interest.

■ ACKNOWLEDGMENTS

D.E. acknowledges the financial support given by the Spanish Ministry of Science, Innovation and Universities under grant nos. PID2019-106383GB-C41 and RED2018-102612-T (MALTA Consolider-Team network) and by the Generalitat Valenciana under grant Prometeo/2018/123 (EFIMAT). C.C. acknowledges support from the Spanish Ministry of Science, Innovation, and Universities under the "Ramon y Cajal" fellowship RYC2018-024947-I. Y.H acknowledges the financial support given by the State Key Laboratory of Precision Spectroscopy, East China Normal University, Shanghai 200062, China

■ REFERENCES

(1) Ali, M. N.; Xiong, J.; Flynn, S.; Tao, J.; Gibson, Q. D.; Schoop, L. M.; Liang, T.; Haldolaarachchige, N.; Hirschberger, M.; Ong, N. P.; Cava, R. J. Large, non-saturating magnetoresistance in WTe2. *Nature* **2014**, *514*, 205.

(2) Pletikosić, I.; Ali, M. N.; Fedorov, A. V.; Cava, R. J.; Valla, T. Electronic Structure Basis for the Extraordinary Magnetoresistance in WTe_2. *Phys. Rev. Lett.* **2014**, *113* (21), 216601.

(3) Wilson, J. A.; Di Salvo, F. J.; Mahajan, S. Charge-density waves and superlattices in the metallic layered transition metal dichalcogenides. *Adv. Phys.* **1975**, *24* (2), 117−201.

(4) Revolinsky, E.; Lautenschlager, E. P.; Armitage, C. H. Layer structure superconductor. *Solid State Commun.* **1963**, *1* (3), 59−61.

(5) Nayak, A. P.; Bhattacharyya, S.; Zhu, J.; Liu, J.; Wu, X.; Pandey, T.; Jin, C.; Singh, A. K.; Akinwande, D.; Lin, J.-F. Pressure-induced semiconducting to metallic transition in multilayered molybdenum disulphide. *Nat. Commun.* **2014**, *5*, 3731.

(6) Liu, Y.; Ang, R.; Lu, W. J.; Song, W. H.; Li, L. J.; Sun, Y. P. Superconductivity induced by Se-doping in layered charge-density-wave system 1T-TaS2−xSex. *Appl. Phys. Lett.* **2013**, *102* (19), 192602.

(7) Berthier, C.; Molinié, P.; Jérome, D. Evidence for a connection between charge density waves and the pressure enhancement of superconductivity in 2H-NbSe2. *Solid State Commun.* **1976**, *18* (9), 1393−1395.

(8) Zunger, A.; Freeman, A. J. Band structure and lattice instability of $TiSe_2$. *Phys. Rev. B: Condens. Matter Mater. Phys.* **1978**, *17* (4), 1839−1842.

(9) Kusmartseva, A. F.; Sipos, B.; Berger, H.; Forró, L.; Tutiš, E. Pressure Induced Superconductivity in Pristine 1*T*−$TiSe_2$. *Phys. Rev. Lett.* **2009**, *103* (23), 236401.

(10) Zhang, Q.; Cheng, Y.; Schwingenschlögl, U. Emergence of topological and topological crystalline phases in TlBiS2 and TlSbS2. *Sci. Rep.* **2015**, *5*, 8379.

(11) Wiegers, G. A. Misfit layer compounds: Structures and physical properties. *Prog. Solid State Chem.* **1996**, *24* (1), 1−139.

(12) Thompson, A. H. The synthesis and properties of 6R-TaS2. *Solid State Commun.* **1975**, *17* (9), 1115−1117.
(13) Riekel, C. Structure refinement of TiSe2 by neutron diffraction. *J. Solid State Chem.* **1976**, *17* (4), 389−392.
(14) Chen, P.; Chan, Y. H.; Fang, X. Y.; Zhang, Y.; Chou, M. Y.; Mo, S. K.; Hussain, Z.; Fedorov, A. V.; Chiang, T. C. Charge density wave transition in single-layer titanium diselenide. *Nat. Commun.* **2015**, *6*, 8943.
(15) Duong, D. L.; Ryu, G.; Hoyer, A.; Lin, C.; Burghard, M.; Kern, K. Raman Characterization of the Charge Density Wave Phase of 1T-TiSe2: From Bulk to Atomically Thin Layers. *ACS Nano* **2017**, *11* (1), 1034−1040.
(16) Bhatt, R.; Bhattacharya, S.; Patel, M.; Basu, R.; Singh, A.; Sürger, C.; Navaneethan, M.; Hayakawa, Y.; Aswal, D. K.; Gupta, S. K. Thermoelectric performance of Cu intercalated layered TiSe2 above 300 K. *J. Appl. Phys.* **2013**, *114* (11), 114509.
(17) Gu, Y.; Katsura, Y.; Yoshino, T.; Takagi, H.; Taniguchi, K. Rechargeable magnesium-ion battery based on a TiSe2-cathode with d-p orbital hybridized electronic structure. *Sci. Rep.* **2015**, *5*, 12486.
(18) Fu, L.; Kane, C. L.; Mele, E. J. Topological Insulators in Three Dimensions. *Phys. Rev. Lett.* **2007**, *98* (10), 106803.
(19) Joe, Y. I.; Chen, X. M.; Ghaemi, P.; Finkelstein, K. D.; de la Peña, G. A.; Gan, Y.; Lee, J. C. T.; Yuan, S.; Geck, J.; MacDougall, G. J.; Chiang, T. C.; Cooper, S. L.; Fradkin, E.; Abbamonte, P. Emergence of charge density wave domain walls above the superconducting dome in 1T-TiSe2. *Nat. Phys.* **2014**, *10*, 421.
(20) Machon, D.; Meersman, F.; Wilding, M. C.; Wilson, M.; McMillan, P. F. Pressure-induced amorphization and polyamorphism: Inorganic and biochemical systems. *Prog. Mater. Sci.* **2014**, *61*, 216−282.
(21) Maczka, M.; Souza Filho, A. G.; Paraguassu, W.; Freire, P. T. C.; Mendes Filho, J.; Hanuza, J. Pressure-induced structural phase transitions and amorphization in selected molybdates and tungstates. *Prog. Mater. Sci.* **2012**, *57* (7), 1335−1381.
(22) ElGhazali, M. A.; Naumov, P. G.; Mu, Q.; Süß, V.; Baskakov, A. O.; Felser, C.; Medvedev, S. A. Pressure-induced metallization, transition to the pyrite-type structure, and superconductivity in palladium disulfide PdS_2. *Phys. Rev. B: Condens. Matter Mater. Phys.* **2019**, *100* (1), No. 014507.
(23) Morosan, E.; Zandbergen, H. W.; Dennis, B. S.; Bos, J. W. G.; Onose, Y.; Klimczuk, T.; Ramirez, A. P.; Ong, N. P.; Cava, R. J. Superconductivity in CuxTiSe2. *Nat. Phys.* **2006**, *2* (8), 544−550.
(24) Rajaji, V.; Janaky, S.; Sarma, S. C.; Peter, S. C.; Narayana, C. Pressure induced topological and structural phase transitions in 1T-TiSe2: a Raman study. *J. Phys.: Condens. Matter* **2019**, *31* (16), 165401.
(25) Mao, H.; Xu, J.-A.; Bell, P. Calibration of the ruby pressure gauge to 800 kbar under quasi-hydrostatic conditions. *J. Geophys. Res.* **1986**, *91* (B5), 4673−4676.
(26) Rodríguez-Carvajal, J. Recent advances in magnetic structure determination by neutron powder diffraction. *Phys. B* **1993**, *192* (1), 55−69.
(27) Errandonea, D.; Segura, A.; Martínez-García, D.; Muñoz-San Jose, V. Hall-effect and resistivity measurements in CdTe and ZnTe at high pressure: Electronic structure of impurities in the zinc-blende phase and the semimetallic or metallic character of the high-pressure phases. *Phys. Rev. B: Condens. Matter Mater. Phys.* **2009**, *79* (12), 125203.
(28) Azaele, S.; Suweis, S.; Grilli, J.; Volkov, I.; Banavar, J. R.; Maritan, A. Statistical mechanics of ecological systems: Neutral theory and beyond. *Rev. Mod. Phys.* **2016**, *88* (3), No. 035003.
(29) Sun, J.; Ruzsinszky, A.; Perdew, J. P. Strongly Constrained and Appropriately Normed Semilocal Density Functional. *Phys. Rev. Lett.* **2015**, *115* (3), No. 036402.
(30) Kresse, G.; Furthmüller, J. Efficient iterative schemes for ab initio total-energy calculations using a plane-wave basis set. *Phys. Rev. B: Condens. Matter Mater. Phys.* **1996**, *54* (16), 11169−11186.
(31) Blöchl, P. E. Projector augmented-wave method. *Phys. Rev. B: Condens. Matter Mater. Phys.* **1994**, *50* (24), 17953−17979.
(32) Cazorla, C.; Errandonea, D.; Sola, E. High-pressure phases, vibrational properties, and electronic structure of $NeHe_2$ and $ArHe_2$: A first-principles study. *Phys. Rev. B: Condens. Matter Mater. Phys.* **2009**, *80* (6), No. 064105.
(33) Alfè, D. PHON: A program to calculate phonons using the small displacement method. *Comput. Phys. Commun.* **2009**, *180* (12), 2622−2633.
(34) Greenberg, E.; Rozenberg, G. K.; Xu, W.; Arielly, R.; Pasternak, M. P.; Melchior, A.; Garbarino, G.; Dubrovinsky, L. S. On the compressibility of ferrite spinels: a high-pressure X-ray diffraction study of MFe2O4 (M = Mg, Co, Zn). *High Pressure Res.* **2009**, *29* (4), 764−779.
(35) Rahman, S.; Saqib, H.; Zhang, J.; Errandonea, D.; Menéndez, C.; Cazorla, C.; Samanta, S.; Li, X.; Lu, J.; Wang, L. Pressure-induced structural and semiconductor-semiconductor transitions in $Co_{0.5}Mg_{0.5}Cr_2O_4$. *Phys. Rev. B: Condens. Matter Mater. Phys.* **2018**, *97* (17), 174102.
(36) Ding, H.; Xu, B. Structural, elastic, and vibrational properties of layered titanium dichalcogenides: A van der Waals density functional study. *J. Chem. Phys.* **2012**, *137* (22), 224509.
(37) Sugai, S.; Murase, K.; Uchida, S.; Tanaka, S. Raman studies of lattice dynamics in 1T-TiSe2. *Solid State Commun.* **1980**, *35* (5), 433−436.
(38) Kieffer, S. W. Thermodynamics and lattice vibrations of minerals: 2. Vibrational characteristics of silicates. *Rev. Geophys.* **1979**, *17* (1), 20−34.
(39) Koley, S. Pressure driven phase transition in 1T-TiSe2, a MOIPT+DMFT study. *Solid State Commun.* **2017**, *251*, 23−27.
(40) Friend, R. H.; Jerome, D.; Yoffe, A. D. High-pressure transport properties of TiS2and TiSe2. *J. Phys. C: Solid State Phys.* **1982**, *15* (10), 2183−2192.
(41) Fang, L.; Wang, Y.; Zou, P. Y.; Tang, L.; Xu, Z.; Chen, H.; Dong, C.; Shan, L.; Wen, H. H. Fabrication and superconductivity of Na_xTaS_2 crystals. *Phys. Rev. B: Condens. Matter Mater. Phys.* **2005**, *72* (1), No. 014534.
(42) Dutta, U.; Malavi, P. S.; Sahoo, S.; Joseph, B.; Karmakar, S. Pressure-induced superconductivity in semimetallic $TiTe_2$ and its persistence upon decompression. *Phys. Rev. B: Condens. Matter Mater. Phys.* **2018**, *97* (6), No. 060503.
(43) Chi, Z.; Chen, X.; Yen, F.; Peng, F.; Zhou, Y.; Zhu, J.; Zhang, Y.; Liu, X.; Lin, C.; Chu, S.; Li, Y.; Zhao, J.; Kagayama, T.; Ma, Y.; Yang, Z. Superconductivity in Pristine $2H_\alpha$−MoS_2 at Ultrahigh Pressure. *Phys. Rev. Lett.* **2018**, *120* (3), No. 037002.
(44) Zhao, X.-M.; Liu, H.-y.; Goncharov, A. F.; Zhao, Z.-W.; Struzhkin, V. V.; Mao, H.-K.; Gavriliuk, A. G.; Chen, X.-J. Pressure effect on the electronic, structural, and vibrational properties of layered 2*H*−$MoTe_2$. *Phys. Rev. B: Condens. Matter Mater. Phys.* **2019**, *99* (2), No. 024111.
(45) Sidorov, V. A.; Nicklas, M.; Pagliuso, P. G.; Sarrao, J. L.; Bang, Y.; Balatsky, A. V.; Thompson, J. D. Superconductivity and Quantum Criticality in $CeCoIn_5$. *Phys. Rev. Lett.* **2002**, *89* (15), 157004.
(46) Wosnitza, J. Quasi-Two-Dimensional Organic Superconductors. *J. Low Temp. Phys.* **2007**, *146* (5), 641−667.

https://doi.org/10.1021/acs.jpclett.1c02492
J. Phys. Chem. Lett. 2021, 12, 9859−9867